NANO LETTERS

LETTER

pubs.acs.org/NanoLett

Hierarchically Porous Graphene as a Lithium−Air Battery Electrode

Jie Xiao,*,† Donghai Mei,† Xiaolin Li,† Wu Xu,† Deyu Wang,† Gordon L. Graff,† Wendy D. Bennett,† Zimin Nie,† Laxmikant V. Saraf,† Ilhan A. Aksay,‡ Jun Liu,*,† and Ji-Guang Zhang*,†

†Pacific Northwest National Laboratory, Richland, Washington 99352, United States

‡Department of Chemical and Biological Engineering, Princeton University, Princeton, New Jersey 08544, United States

Supporting Information

ABSTRACT: The lithium−air battery is one of the most promising technologies among various electrochemical energy storage systems. We demonstrate that a novel air electrode consisting of an unusual hierarchical arrangement of functionalized graphene sheets (with no catalyst) delivers an exceptionally high capacity of 15000 mAh/g in lithium−O_2 batteries which is the highest value ever reported in this field. This excellent performance is attributed to the unique bimodal porous structure of the electrode which consists of microporous channels facilitating rapid O_2 diffusion while the highly connected nanoscale pores provide a high density of reactive sites for Li−O_2 reactions. Further, we show that the defects and functional groups on graphene favor the formation of isolated nanosized Li_2O_2 particles and help prevent air blocking in the air electrode. The hierarchically ordered porous structure in bulk graphene enables its practical applications by promoting accessibility to most graphene sheets in this structure.

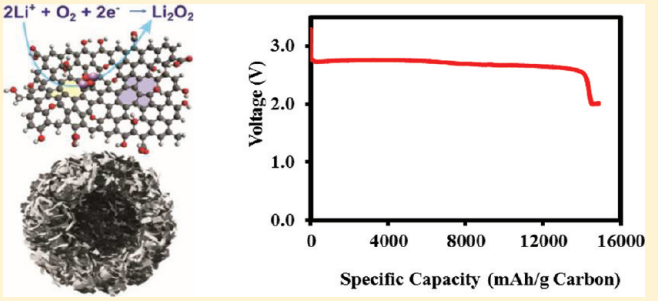

KEYWORDS: Li−air battery, graphene, specific energy, Li_2O_2, O_2 reduction

Lithium-ion batteries have been widely used in many electronic devices that are important to our daily life. However, after a steady improvement of ∼10−15% during the last two decades, the energy density of lithium-ion batteries is now approaching its theoretical limit set by the energies of cathode and anode materials used in these batteries.[1,2] Therefore, in recent years, the pursuit of the next generation of energy storage systems has been intense globally.[1−4] Among various electrochemical energy storage systems explored to date, the lithium−air (Li−air) battery is one of the most promising technologies, with a theoretical energy density nearly 10 times that of conventional lithium-ion batteries.[5−7] This is because lithium metal as an anode has a capacity 10 times higher than that of conventional graphite anodes, and oxygen as the cathode of a Li−air battery can be absorbed freely from the environment leading to a significant reduction in the weight and the cost of the battery.

The performance of Li−air batteries is affected by many factors such as relative humidity,[8] oxygen partial pressure,[9] choice of catalysts,[10] electrolyte composition,[11] the macrostructure of the air electrode,[12,13] the micro- to nanostructure of carbonaceous materials,[14] and overall cell designs.[8,15] Precipitation of reaction products (such as Li_2O_2) on the carbonaceous electrode eventually blocks the oxygen pathway and limits the capacity of the Li−air batteries. Therefore, there is a critical need to design an optimum air electrode containing micrometer-sized open porosity for rapid oxygen diffusion and substantial nanoporosity (2−50 nm) to catalyze Li−O_2 reactions while preventing excessive growth of the discharge products that block chemical pathways.

In this work, we use a colloidal microemulsion approach and demonstrate, for the first time, the construction of hierarchically porous air electrodes with functionalized graphene sheets (FGSs) that contain lattice defects and hydroxyl, epoxy, and carboxyl groups.[16] Figure 1 shows the schematic structure of functionalized graphene[16] with an ideal bimodal porous structure which is highly desirable for Li−O_2 battery operation. Although graphene sheets and composites have been studied as electrode materials for Li−ion batteries,[17−19] they typically form a two-dimensional (2D) layered structure that is not suitable for Li−air battery application. On the contrary, the three-dimensional (3D) air electrodes developed in this work consist of interconnected pore channels on both the micro- and nanometer length scales. High capacities of these air electrodes have been correlated with their bimodal pore structures. Further, modeling by density functional theory (DFT) and electron microscopy characterization suggests that lattice defect sites on the functionalized graphene play a critical role in the formation of small, nanometer-sized discharge products (Li_2O_2). The combination of the hierarchical pore structure and the effect of the defects during the discharge process produces an exceptionally high capacity of 15000 mAh/g, which is the highest value ever reported in this field.

Morphology of As-Prepared Graphene-Based Air Electrodes. Graphene and graphene-based composites have been studied as electrode materials for supercapacitors,[17] Li-ion

Received: September 25, 2011

   dx.doi.org/10.1021/nl203332e | *Nano Lett.* XXXX, XXX, 000–000

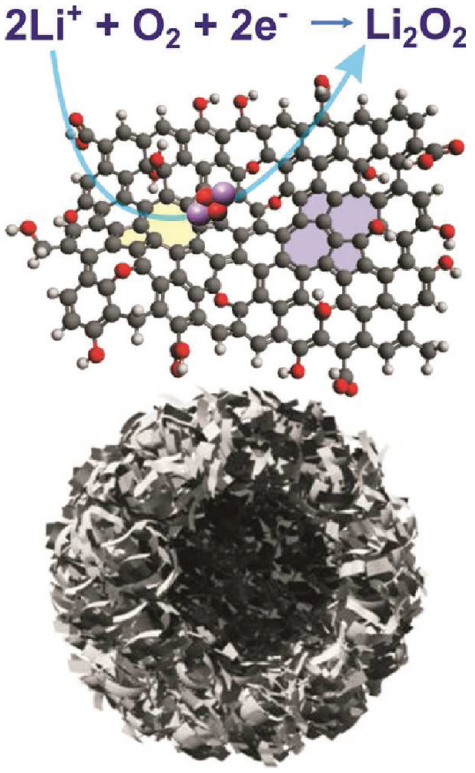

Figure 1. Schematic structure of a functionalized graphene sheet (upper image) with an ideal bimodal porous structure (lower image) which is highly desirable for Li−O_2 battery operation. Functional groups and lattice defects on FGSs showing epoxy and hydroxyl groups on both sides of the graphene plane, carboxyl, and hydroxyl groups at the edges, a 5−8−5 defect (yellow), and a 5−7−7−5 (Stone−Wales) defect (blue). Carbon atoms are gray, oxygen atoms are red, and hydrogen atoms are white.[16] Lattice defect sites such as the 5−8−5 are energetically favorable sites for the nucleation and pinning of the reaction products (i.e., Li_2O_2).

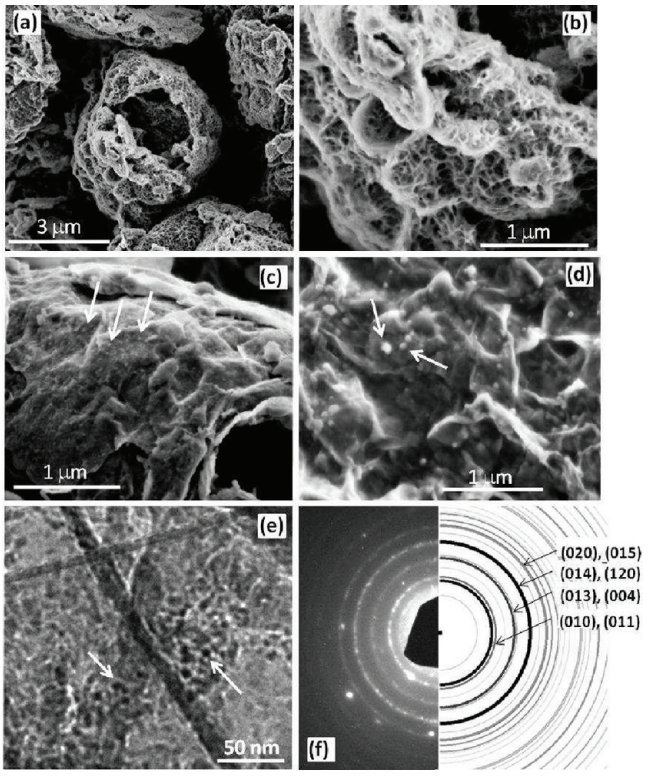

Figure 2. Morphologies of the graphene-based air electrode. (a, b) SEM images of as-prepared FGS (C/O = 14) air electrodes at different magnifications. (c, d) Discharged air electrode using FGS with C/O = 14 and C/O = 100, respectively. (e) TEM image of discharged air electrode consisting of FGS with C/O = 14. The white arrows point out the deposited Li_2O_2 particles on FGS surfaces. (f) SAED pattern of the particles on FGS with C/O = 14.

batteries,[18] and proton-exchange membranes for fuel cells (PEM).[19] In almost all these studies, the graphene sheets readily restack due to either van der Waals or capillary forces and form 2D structures that hinder the rapid gas diffusion that is essential for the efficient operation of Li-air batteries.[20] Our work reveals for the first time that FGSs, if manipulated appropriately, can self-assemble into highly porous, 3D architectures with interconnected pore channels. These architectures are not only useful for Li−air batteries but also important for many other energy storage, conversion, and catalytic applications.

FGS used in this study was produced by the thermal expansion and simultaneous reduction of graphite oxide.[21,22] While graphite oxide has a C/O ratio of ∼2, after thermal reduction at 1050 °C for 30 s, the C/O ratio of the FGS increases to ∼15 as a result of CO_2 release. With longer residence times, this ratio can be increased to values as high as 300. With the release of CO_2, lattice defects form. The degree of defect formation and surface functionalization on the graphene sheets correlates with the C/O ratio.[21−24] The C/O ratio reflects the relative content of the lattice defects and/or oxygen functional groups on the graphene sheets. The smaller the C/O ratio, the higher the number of functional groups/lattice defects on the FGS. When the C/O ratio increases from 15 to 100, the electrical conductivity of pellets produced with FGS also increases by approximately 2-fold from ∼10^4 to 2 × 10^4 S/m (see supplementary Figure S1, Supporting Information).

To produce the FGS-based air electrodes, FGS was first dispersed in a microemulsion solution which also contained the binder materials (DuPont Teflon PTFE-TE3859 fluoropolymer resin aqueous dispersion, 60 wt % solids) for the electrode. After casting and drying, very unusual morphologies were produced as shown in panels a and b of Figure 2. Surprisingly, FGSs aggregated into loosely packed, "broken egg" structures leaving large interconnected tunnels that continue through the entire electrode depth (Figure 2a). These tunnels can function as numerous arteries that continuously supply oxygen into the interior of the electrode during the discharge process. More importantly, the complex pore structure is retained after electrolyte infiltration, unlike other porous carbon materials tested. Higher magnification observation of the "shells" of the "broken eggs" (Figure 2b) reveals that the "shells" consist of numerous smaller nanoscale pores contiguous with the large tunnels. This unique morphology is an ideal design for an air electrode. During discharge the robust large tunnels can function as "highways" to supply the oxygen to the interior parts of air electrode while the small pores on the walls are the "exits" which provide triphase (solid−liquid−gas) regions required for oxygen reduction.[8,9,12]

The formation of this unique and useful FGS morphology results from the mixing step in which an aqueous poly(tetrafluoroethylene) (PTFE) microemulsion is added to the FGSs. Significant foaming occurs during mixing, resulting in a

dx.doi.org/10.1021/nl203332e |Nano Lett. XXXX, XXX, 000–000

distribution of bubble sizes ranging in diameter from tens of nanometers to tens of micrometers (see supplementary Figure S2, Supporting Information). In many cases the large bubbles contain numerous smaller-diameter bubbles. The hydrophobic nature of the FGS surfaces forces the particles to assemble in the surfactant-rich "skin" of each bubble. Upon drying, the FGS forms a carbonaceous replica of the foam, resulting in the final interconnected structure containing large tunnels and small pores. FGS has not only a unique 2D macromolecular structure but also a hydrophobic plane (when its C/O > 10) which enables the assembly of the hierarchical structures at the liquid/gas interfaces.

Earlier, we applied the same approach on Ketjenblack (KB) carbon (EC-600JD, Nobel Polymer Chemicals, Chicago, IL).[12] However, the morphologies of the KB-based air electrode are quite different from the graphene ones even when we use the same preparation approach. Since porous KB has a much larger particle size than that of the molecularly thin graphene sheets, most of the PTFE microemulsion is absorbed into the pores instead of interacting with carbonaceous material on the interface of the bubbles. Accordingly, the discharge capacity of the KB-based air electrode is much lower than that of FGS-based air electrode.

The N_2 adsorption isotherm and the BJH pore size distribution are shown in Figure S3 (Supporting Information). The N_2 adsorption isotherm of the FGS electrode shows a type II curve with a H3 hysteresis loop according to the IUPAC classification. The absence of saturation at unity pressure on the adsorption curve shows the presence of macropores larger than 100 nm. The hysteresis in the middle pressure range suggests the existence of slit-type meso- or nanoporosity typically formed by aggregates of platelike particles.[25] The microporosity is not analyzed here. The size in the hysteresis loop is related to the mesopore volume and the connectivity of the pores.[26] The BJH pore size distribution, although not accurate for this type of complex pore geometries, does show the continuous presence of a wide range of porosity from nanometer to a few hundred nanometer scales. The average pore size calculated from Figure S3 (Supporting Information) is about 18 nm, within the pore-size range typically found in a high-capacity air electrode.[13] The pore volume and surface area of the air electrode are 0.84 cm^3/g and 186 m^2/g, respectively. The surface area of the electrode decreased from the FGS powder (590 m^2/g) because of the addition of Teflon binder.

The processing method described above was used to prepare the air electrodes with FGSs of two different C/O ratios (14 and 100) resulting in similar final morphologies (see supplementary Figure S4 in the Supporting Information for the morphology of the air electrode consisting of FGS with C/O = 100). Although the overall cathode structures were alike, the morphologies of the reaction products that formed during discharge on the two surfaces were quite different. Panels c and d of Figure 2 compare the surface morphologies of the discharged air electrodes using graphene with C/O = 14 and 100, respectively. In both cases, the primary discharge product formed on the graphene surfaces was Li_2O_2 as confirmed by X-ray diffraction (XRD) (see supplementary Figure S5, Supporting Information) and selected area electron diffraction (SAED) (Figure 2f) of the particles (~10 nm) on FGS (C/O = 14) shown in the higher magnification transmission electron microscopy (TEM) image of Figure 2e. Unlike conventional carbonaceous electrodes in which a dense, thick layer of large Li_2O_2 particles is typically formed on the electrode surface, the Li_2O_2 particles deposited on FGS are nanometer-sized and isolated (panels c, d, and e of Figure 2). There is no evidence of large particle formation that blocks the air channels. Further observation showed that the deposited Li_2O_2 particles were consistently smaller on the graphene with a lower C/O ratio (C/O = 14) than FGS with a higher C/O ratio (C/O = 100). Figure 2d also shows fewer Li_2O_2 particles in the air electrode made from FGS with C/O = 100, with a corresponding increase in size and spacing between precipitates. These observations suggest that differences in Li_2O_2 nucleation and growth are likely related to the lattice defects and/or functional groups, existing on the different FGSs as discussed later in this work.

To further verify the utility of the hierarchical pore organization, we also prepared a "paper-like" FGS electrode by filtration of an FGS dispersion and tested it as an air electrode under identical conditions. During evaporative drying of the filtered material, capillary forces restack the high-aspect-ratio graphene sheets and form 2D electrode structures that severely inhibit oxygen and electrolyte diffusion. (See supplementary Figure S6 in the Supporting Information.) Such cathodes had capacities of only less than 100 mAh/g, providing further support for the unique aspects of the hierarchical and contiguous pore organization to achieve the observed electrochemical performance with these FGS materials.

Electrochemical Performance of Li−Air Batteries Using Graphene Electrodes. Figure 3a shows the discharge curve of a $Li-O_2$ cell utilizing an air electrode prepared with FGS of C/O = 14 and tested in pure oxygen at an initial pressure of ~2 atm (the pressure will decrease during discharge because of oxygen consumption). Surprisingly, the discharge capacity reaches 15000 mAh/g carbon with a plateau at around 2.7 V. The corresponding specific energy is 39714 Wh/kg carbon, giving an average voltage of 2.65 V. This is the highest capacity reported to date for nonaqueous $Li-O_2$ batteries.[27−29] These results are highly repeatable with multiple parallel test results showing similar capacity under the same test conditions. To exclude possible electrochemical contributions from the decomposition of organic functional groups on the graphene sheets, the electrode produced with the FGS paper was also discharged to 2.0 V in pure argon as shown in Figure 3b. Clearly, any capacity contribution arising from the functional groups can be ignored (<40 mAh/g) within the voltage range in this work. To minimize the electrolyte decomposition as observed in $Li-O_2$ batteries when carbonate solvent based electrolytes were used,[30,31] ether-based electrolyte (LITFSI in tri(ethylene glycol) dimethyl ether (Triglyme)) was used in this work. As discussed above, a significant amount of Li_2O_2 has been observed (see Figure S52 in the Supporting Information and Figure 2f), which is consistent with the formation of Li_2O_2 by other groups when ether-based electrolytes were used in $Li-O_2$ cells.[32,33]

To further evaluate their potential for practical application, Li−air batteries were tested in a pouch-type cell configuration (see inset of Figure 3c) in which the polymeric pouch was used to regulate O_2 and H_2O ingress.[8,34] The pouch cell was operated in the ambient environment with an oxygen partial pressure of 0.21 atm and 20% relative humidity. The resulting discharge curve for the cell is shown in Figure 3c. At the same current density of 0.1 mA/cm^2, the specific capacity based on the carbon weight exceeded 5000 mAh/g. This further confirms the unique contribution of the hierarchical pore structure on performance. Other possible contributions to the unprecedented performance include (i) the superior electronic conductivity of graphene and (ii) the appropriate choice of a noncarbonate based electrolyte.[35−37]

dx.doi.org/10.1021/nl203332e |Nano Lett. XXXX, XXX, 000–000

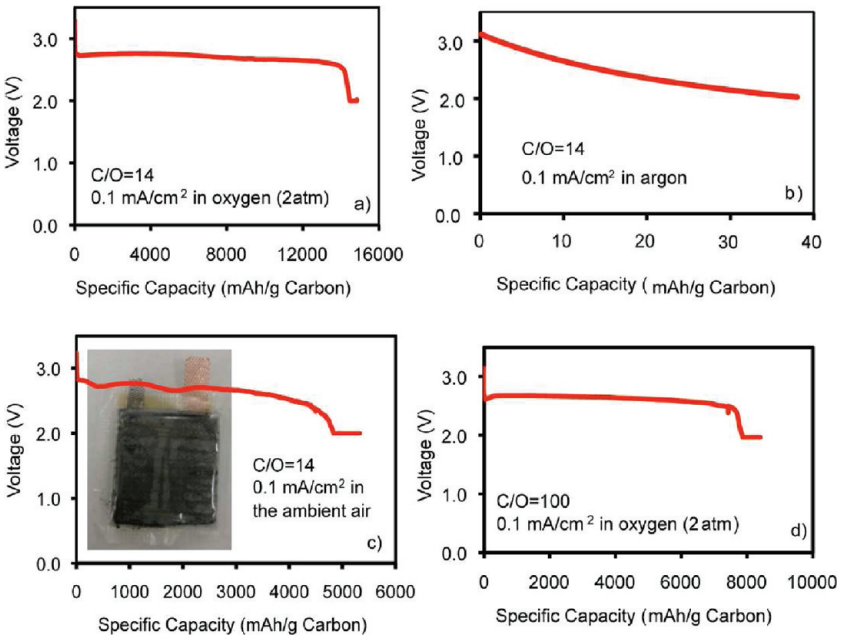

Figure 3. Electrochemical performances of Li−air batteries using FGS as the air electrodes. (a) The discharge curve of a Li−O_2 cell using FGS(C/O = 14) as the air electrode (P_{O_2} = 2 atm). (b) The same Li−O_2 cell as in (a) but tested in the pure argon atmosphere. (c) Discharge curve of a pouch-type Li−air cell made from FGS (C/O = 14) operated in ambient environment (P_{O_2} = 0.21 atm, relative humidity = 20%). The inset shows the prototype of the pouch cell. (d) The discharge curve of a Li−O_2 cell using FGS (C/O = 100) as the air electrode (P_{O_2} = 2 atm).

Table 1. DFT Calculated Binding Energies of $(Li_2O_2)_n$ Clusters on the Perfect and the 5−8−5 Defect Graphene Surfaces with Functional (CCOH) Group

	binding energy, E^b (eV)		
cluster	perfect graphene	5−8−5 defect graphene	5−8−5 defect graphene with COOH group
Li_2O_2	−0.26	−0.70	−0.90
$(Li_2O_2)_2$	−1.15	−1.27	−0.82
$(Li_2O_2)_3$	−1.60	−1.77	−0.90
$(Li_2O_2)_6$	−1.85	−2.08	−1.18

Figure 3d shows the discharge curve measured on Li−O_2 batteries with cathodes fabricated from FGS with a C/O ratio of 100 (C/O = 100). The capacity delivered from FGS with reduced defect/functional group concentrations is approximately one-half that of cathodes synthesized from FGS with greater number density of combined lattice defects and the functional sites (C/O = 14, Figure 3a). This finding is consistent with the observed Li_2O_2 particle densities observed in the scanning electron microscopy (SEM) and TEM images shown in panels c and d of Figure 1 and is further supported by the DFT modeling presented below. Preferred growth, or aggregation, of Li_2O_2 on defect regions of the FGS (defects) is further investigated in the following section.

Deposition Mechanism of Li_2O_2 on the Graphene Surface. To better understand the deposition mechanism of Li_2O_2 particles on FGS during discharge on the molecular level, periodic DFT calculations were performed using the Vienna ab initio simulation package (VASP).[37,38] To account for the possible effects induced by the defect sites on the FGS, we calculated the interactions of various sizes of Li_2O_2 clusters on the graphene substrate with a 5−8−5 defect site. To account for possible functionalized groups on the graphene sheet, we also calculated, as an example, the interactions of adsorbed $(Li_2O_2)_n$ clusters on the 5−8−5 defect graphene substrate with a pre-existing COOH group. The interaction (binding) energies between the $(Li_2O_2)_n$ cluster and the supported graphene surfaces calculated from DFT are summarized in Table 1, and the corresponding optimized structures of $(Li_2O_2)_n$ cluster/graphene are shown in Figure 4. Calculations were also performed on other defect structures and functional groups with similar findings, and the results are not included here due to space limitations.

The DFT results show only weak interactions between the Li_2O_2 monomer and graphene substrate, similar to a physical adsorption mechanism. The calculated binding energy of the Li_2O_2 monomer is only −0.26 eV (Table 1). However, this interaction becomes much stronger (−0.70 eV) if the Li_2O_2 monomer binds at the vicinity of a 5−8−5 defect site on the graphene surface (−0.7 eV), and even stronger on COOH groups associated with the defects (−0.9 eV), indicating that the Li_2O_2 particles most likely prefer to nucleate and grow around the defective sites with functional groups in FGS. With increasing $(Li_2O_2)_n$ cluster size, the binding energy between the Li_2O_2 nanocluster and the FGS generally increases. Since the binding energy is related to the stability of the earlier nuclei on the surface, the theoretical findings suggest that the cathode structure can be optimized by tailoring the number and positions of the defects and functional groups on the graphene. Because we only tackle the very beginning stage of nucleation, the structure of the formed Li_2O_2 particle (up to $Li_{12}O_{12}$) is amorphous. As shown in Figure 4, the preferred growth mode, however, is most likely 2D (flatly covering the graphene support) instead of 3D. After the nucleation, the most exposed surface orientation of the Li_2O_2 particle is the (100) structure.[39]

dx.doi.org/10.1021/nl203332e |*Nano Lett.* XXXX, XXX, 000–000

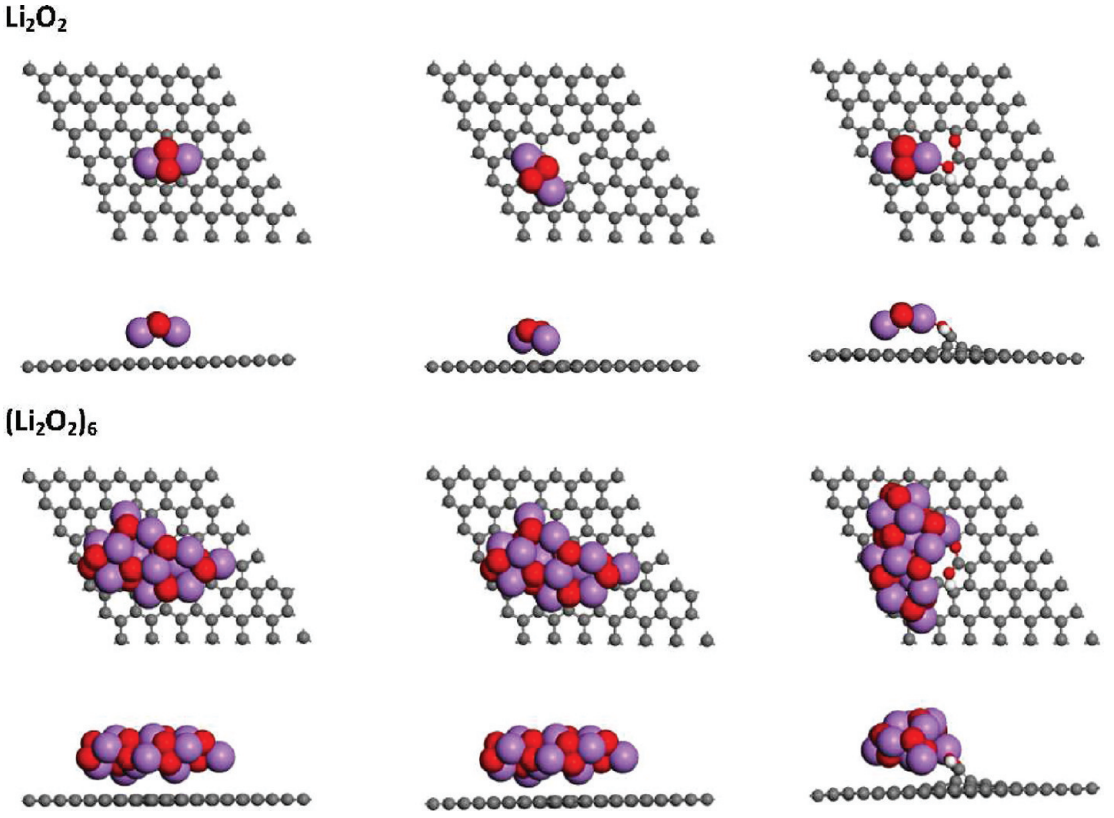

Figure 4. Top and side views of optimized structures of Li_2O_2 and $(Li_2O_2)_6$ clusters on perfect graphene (left column), the 5−8−5 defect graphene (middle column), and the 5−8−5 defect graphene with bound COOH group (right column). In each structure, the top and side views are shown in the upper and the lower panel, respectively. The color scheme is as follows: carbon atoms are in gray, lithium atoms are in purple, and oxygen atoms are in red.

To further describe the system, an aggregation model patterned after the work of Mei et al.[40] was applied to the Li_2O_2−graphene composite. Here, we simulate the Li_2O_2 aggregation process on the graphene surface as a reaction of an adsorbed Li_2O_2 monomer with an existing $(Li_2O_2)_{n-1}$ $(n \geq 2)$ cluster:

$$(Li_2O_2)_{n-1} + Li_2O_2 \rightarrow (Li_2O_2)_n \quad (1)$$

The driving force for this aggregation process is then represented by the free energy change

$$\Delta G = G_{(Li_2O_2)_n} - G_{(Li_2O_2)_{n-1}} - G_{Li_2O_2} \quad (2)$$

Assuming the $\Delta(TS)$ and $\Delta(PV)$ terms (where T is the temperature, S is the entropy, P is the pressure, and V is the volume) have negligible contribution to the free energy change because of the condensed phases involved, ΔG can be calculated using the following equation

$$\Delta G = E^{b}_{(Li_2O_2)_n} - E^{b}_{(Li_2O_2)_{n-1}} - E^{b}_{Li_2O_2} \quad (3)$$

A negative value of ΔG indicates an energetically favorable process. As indicated in eq 3, the aggregation process depends upon the binding energy of an isolated Li_2O_2 monomer. Figure 5 shows the free energy changes of Li_2O_2 aggregation on both defect-free and 5−8−5 defect graphene surfaces with and without pre-existent COOH surface groups. For the pristine graphene surface, the aggregation of adsorbed Li_2O_2 monomers is energetically favorable until the formation of $(Li_2O_2)_5$ clusters,

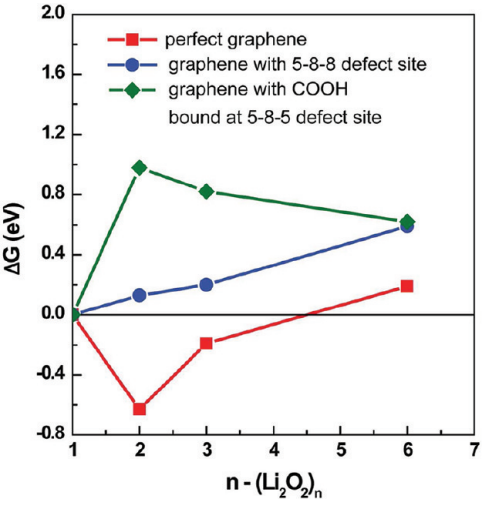

Figure 5. Calculated free-energy change as a function of aggregated $(Li_2O_2)_n$ cluster size. The negative value of ΔG indicates an energetically more favorable aggregating process. On the perfect graphene surface, the aggregation of adsorbed Li_2O_2 monomer is energetically favorable up to $(Li_2O_2)_5$, while it is energetically unfavorable from the beginning on the 5−8−5 defect graphene surface with or without a functional group (COOH).

while further aggregation to the larger $(Li_2O_2)_n$ $(n > 5)$ becomes energetically unfavorable. This is due to the fact that the interaction between the Li_2O_2 monomer and the perfect

dx.doi.org/10.1021/nl203332e |*Nano Lett.* XXXX, XXX, 000–000

graphene is very weak. The isolated Li_2O_2 monomers easily migrate and aggregate on the perfect graphene sheets. However, when the $(Li_2O_2)_n$ cluster becomes larger, the interaction between the formed $(Li_2O_2)_n$ clusters and the substrate increases thus resisting further $(Li_2O_2)_n$ aggregation. In comparison, aggregation is energetically unfavorable at all cluster sizes on the 5−8−5 defect site with and without the pre-existent COOH group because of the greater binding strength for the adsorbed Li_2O_2 monomer at either the vicinity of the defect site or directly with the COOH group. It is expected that the migration of the Li_2O_2 monomer becomes more difficult on the 5−8−5 defective graphene surfaces. Therefore, the $(Li_2O_2)_n$ cluster prefers to be isolated on the lattice defects of graphene with and without functional groups rather than combining to form larger Li_2O_2 nanoparticles, which is consistent with the SEM and TEM images. Although the DFT calculation is only limited to very small clusters that likely exist in the early nucleation process, the predicted trend provides a clue to our experimental observations. On FGS with C/O = 14, the particle sizes of Li_2O_2 on the defects are only10−20 nm since the aggregation of Li_2O_2 is prevented by the strong interaction between the defect sites on FGS and the Li_2O_2 monomers. For FGS with C/O = 100, fewer and larger Li_2O_2 particles are observed (Figure 2d) and the particle size distribution is less homogeneous. The larger particles in Figure 2d could result from Li_2O_2 cluster aggregation on the pristine graphene regions (where energetically favored) while the smaller nuclei form near FGS defects where aggregation is energetically unfavorable or more rapid growth due higher diffusion rates of the atomic species on the FGS. Currently the calculations suggest that both lattice defects and functional groups increase the interfacial binding and prevent agglomeration. Since C/O = 14 graphene has more functional groups and fewer lattice defects than C/O = 100 graphene, the better performance and smaller Li_2O_2 particles in the C/O = 14 graphene electrode suggest that the functional group plays a more important role than the lattice effect.

Understanding the roles of the lattice defects and the functional groups on the graphene substrate is very important for the Li−air battery system. Since Li_2O_2 has preferred growth points and the particle size is limited by the defects, it may be possible to tune the energy/power ratio for specific energy applications through control of the defects and functional groups on the graphene surface. Such structure control could be highly advantageous for rechargeable Li−air cells. For future research on rechargeable Li−air batteries it is also critical to identify appropriate catalysts to reduce the oxidation overpotential of Li_2O_2. However, because both Li_2O_2 and the catalyst are solids and the former disappears repeatedly after each charging, a method to maintain a good contact between Li_2O_2 and the catalyst through a long-term cycling remains a challenge. Since Li_2O_2 prefers to nucleate near the defects and functional groups, it is feasible to attach the catalysts close to those functional groups which may address the contact issue for the rechargeable Li−air batteries. The recent discovery of the triple junction structure in which a metal catalyst is stabilized at the metal−metal oxide defected graphene surface may provide some clues on how to design such catalyst systems for Li−air batteries.[19] It is also possible that those defects and functional groups themselves may have certain catalytic effects on the oxygen reduction reactions. However, since Li_2O_2 nucleation is also involved in the oxygen reduction, the catalytic effect of the defects cannot be easily differentiated from the DFT calculations. More detailed studies using a combination of electrochemical and theoretical approaches are needed to further understand the functions of the defects.

In summary, primary Li−air batteries containing hierarchically porous FGS deliver an extremely high capacity of 15000 mAh/g, highlighting the potential application of graphene in the metal−air system. This electrode design also shines light on how to control the architecture and surface chemistry of the carbon electrode for rechargeable Li−O_2 batteries. Two critical factors are responsible for the significantly improved performance of the graphene-based air electrode. One is the unique morphology of the graphene-based air electrode in which numerous large tunnels facilitate continuous oxygen flow into the air electrode while other small "pores" provide ideal triphase regions for the oxygen reduction. Another important factor is related to the Li_2O_2 deposition mechanism on the graphene surface. DFT calculations show that Li_2O_2 prefers to nucleate and grow near functionalized lattice defect sites on graphene with functional groups as a result of the relatively stronger interaction between the deposited Li_2O_2 monomer at the 5−8−5 defects. Most importantly, consistent with the experiments, the changes in free energy as a function of the size of Li_2O_2 cluster suggest that in the vicinity of those defective sites the aggregation of Li_2O_2 clusters is energetically unfavorable; therefore the deposited Li_2O_2 would form the isolated nanosized "islands" on FGS, further ensuring smooth oxygen transport during the discharge process. Limited size or thickness of the reaction products with preferred growth points may also improve the rechargeability of Li−air batteries because it prevents continuous increase in electrode impedance and provides better access for a catalyst during the charging process.

Methods. *Air Electrode Preparation.* The air electrode was prepared by a dry rolling process described in our previous work.[11] Functionalized graphene sheets were provided by Vorbeck Materials Corp., Jessup, MD, USA (under the trade name of Vor-x) and contain lattice defects[22] and oxygen (epoxy, hydroxyl, and carboxyl) functional groups with an approximate C/O ratio of 14 or 100.[23,24] In as-produced form, FGS contains approximately 80% single-sheet graphene along with stacked graphene (graphene stacks) as described previously.[23,24] The weight ratio between FGS (or Vor-x) and PTFE binder was controlled at 75:25. The final loading of graphene in the electrode was 2.1 mg/cm^2. The thickness of the graphene-based air electrode was 0.035 cm. To investigate the hierarchical porosity effect in a graphene-based air electrode, a paper-like FGS electrode was also prepared by a filtration method for comparison. In this case FGS (∼10 mg) and cetyl trimethylammonium bromide (CTAB, 0.2 g) were added into 10 mL water and sonicated for 30 min to form a homogeneous suspension. Then the suspension (1 mL) was filtered, washed with ethanol, and dried in ambient conditions. The graphene film was peeled off the membrane and used directly as the air electrode.

Physical Characterization. The structure of the discharged products was characterized by using a Philips X'Pert X-ray diffractometer in a $\theta-2\theta$ scan mode and Cu Kα radiation at λ = 1.54 Å. The discharged graphene-based air electrode was scanned at 2°/min between 10 and 80°. A JEOL 5900 SEM equipped with a Robinson series 8.6 backscattered electron detector and an EDAX Genesis energy-dispersive spectroscopy (EDS) system with a Si (Li) EDS detector was used to investigate the particle morphology. The optical microscope images were taken by using a Meiji metallurgical microscope (model MX8530) with a

dx.doi.org/10.1021/nl203332e |*Nano Lett.* XXXX, XXX, 000–000

PAXcam digital microscope camera using PAX-it image software. Images were taken with transmitted light using a 200× objective.

Electrochemical Tests. The Li−air coin cells (Type 2325 coin cell kits from CNRC, Canada) were assembled in an argon-filled glovebox (MBraun Inc.) with moisture and oxygen content of less than 1 ppm. The positive pans of the 2325 coin cells were 19 machine-drilled holes that were evenly distributed on the pans to allow air passage.[6] Lithium disks (1.59 cm diameter and 0.5 mm thick) were used as the anode. The electrolyte was prepared by dissolving 1 mol of lithium bis(trifluoromethanesulfonyl)imide (LITFSI) in tri(ethylene glycol) dimethyl ether (Triglyme). The salts and solvents used in the electrolyte were all battery-grade materials from Ferro Corp. A Whatman GF/D glass microfiber filter paper (1.9 cm diameter) was used as the separator. For the cells tested in the oxygen environment the customized coin cells were placed in a PTFE container filled with pure oxygen (2 atm). For the cells tested in ambient environment, pouch cells were used to evaluate the graphene-based air electrode as described in our earlier publication.[7] A heat-sealable polymer (Melinex 301H, DuPont Teijin Films, Wilmington, DE) was used as both the packaging and oxygen-diffusion membrane. Melinex 301H is a bilayer membrane with a biaxially oriented poly(ethylene terephthalate) (PET) layer, and a terephthalate/isophthalate copolyester of ethylene glycol thermal bonding layer. The pouch cells were heat sealed at 140−200 °C under constant pressure. The weight ratio between the electrolyte and graphene in the air electrode is 31, which was measured during the assembly process of the pouch cells. The electrochemical tests were performed at room temperature in an Arbin BT-2000 battery tester. A current density of 0.1 mA/cm^2 was used for all the tests. The cells were discharged to 2.0 V and then held at 2.0 V until the current density decreased to less than $I/5$ = 0.02 mA/cm^2.

Computational Details. Periodic DFT calculations were performed using the Vienna ab initio simulation package (VASP).[37,38] The projector augmented wave (PAW) method combined with a plane-wave basis set and a cutoff energy of 400 eV was used to describe core and valence electrons.[41,42] The Perdew−Burke−Ernzerhof (PBE) form of generalized gradient approximation (GGA)[43] with spin polarization was implemented in all calculations. Ground-state atomic geometries of the entire systems were obtained by minimizing the forces on each atom to below 0.05 eV/Å. The graphene substrate was modeled as a single sheet with (6 × 6) supercell (Figure 4a). A 15 Å thick vacuum layer was inserted between two sheets in the z direction. After different Brillouin k-point samplings for systems studied here were tested, a (3 × 3 × 1) k-point sampling scheme was applied to reach the accuracy of the calculations. The graphene substrate with a 5−8−5 defect site (Figure 4b) and the preexistent functional group (COOH) (Figure 4c) were also studied.[44]

The binding energies (E^b) of $(Li_2O_2)_n$ (n = 1−6) clusters with the perfect and defected (with COOH) graphene substrates were calculated.

$$E^b = [E_{(Li_2O_2)_n + \text{graphene}} - (nE_{Li_2O_2} + E_{\text{graphene}})]/n \qquad (4)$$

where $E_{(Li_2O_2)+\text{graphene}}$ is the total energy of the interacting system of the graphene substrate and the supported $(Li_2O_2)_n$ cluster, E_{graphene} is the total energy of the optimized bare graphene surface slab, and $E_{(Li_2O_2)}$ is the energy of a Li_2O_2 monomer in vacuum. The more negative the E^b value, the stronger the interaction between the $(Li_2O_2)_n$ cluster and graphene is.

■ ASSOCIATED CONTENT

Supporting Information. Additional supporting figures. This material is available free of charge via the Internet at http://pubs.acs.org.

■ AUTHOR INFORMATION

Corresponding Author

*E-mail: jiguang.zhang@pnnl.gov, jun.liu@pnnl.gov, jie.xiao@pnnl.gov.

Author Contributions

J.Z., J.L. and J.X. conceived and designed the experiments. D.M. carried out the modeling calculations. J.X., X.L., and D.W. were involved in the electrode preparation and cell assembly. W.X. prepared the electrolyte. W.D.B. did the microscopic work. J. L., G.L.G., Z.N., L.V.S., and I.A.A. did the characterization. J.Z., J.L., D.M., I.A.A., and J.X. cowrote the manuscript. G.L.G. edited the manuscript.

■ ACKNOWLEDGMENT

The authors thank L. Kovarik and C. M. Wang of Pacific Northwest National Laboratory (PNNL) for the TEM characterization. Funding from the Laboratory Directed Research and Development Program at PNNL is also greatly appreciated by the authors. The TEM work was performed at the Environmental Molecular Sciences Laboratory, a national scientific user facility sponsored by the Department of Energy (DOE) Office of Biological and Environmental Research and located at PNNL. The DOE Office of Basic Energy Sciences, Division of Materials Sciences and Engineering, also provided support under Award KC020105-FWP12152 for the modeling and understanding of the structure of the materials. The computing time was made available through a Computational Catalysis Grand Challenge project (gc34000) and the National Energy Research Scientific Computing Center (NERSC). I.A.A. also acknowledges support from ARO/MURI Grant No. W911NF-09-1-0476.

■ REFERENCES

(1) Johnson, C. S.; Li, N.; Vaughey, J. T.; Hackney, S. A.; Thackeray, M. M. Lithium manganese oxide electrodes with layered-spinel composite structures $xLi_2MnO_3 \cdot (1-x)Li_{1+y}Mn_{2-y}O_4$ ($0 < x < 1, 0 < y < 0.33$) for lithium batteries. *Electrochem. Commun.* **2005**, *7*, 528.

(2) Whittingham, M. S. Lithium batteries and cathode materials. *Chem. Rev.* **2004**, *104*, 4271–4301.

(3) USCAR—United States Council for Automotive Research LLC. http://www.uscar.org

(4) Girishkumar, G.; McCloskey, B.; Luntz, A. C.; Swanson, S.; Wilcke, W. Lithium−air battery: promise and challenges. *J. Phys. Chem. Lett.* **2010**, *1*, 2193–2203.

(5) Abraham, K. M.; Jiang, Z. A polymer electrolyte-based rechargeable lithium/oxygen battery. *J. Electrochem. Soc.* **1996**, *143*, 1–5.

(6) Lu, Y. C.; Gasteiger, H. A.; Parent, M. C.; Chiloyan, V.; Horn, Y. S. The influence of catalysts on discharge and charge voltages of rechargeable Li−oxygen batteries. *Electrochem. Solid State Lett.* **2010**, *13*, A69–A72.

(7) Zheng, J. P.; Liang, R. Y.; Hendrickson, M.; Plichta, E. J. Theoretical energy density of Li−air batteries. *J. Electrochem. Soc.* **2008**, *155*, A432–A437.

(8) Zhang, J.-G.; Wang, D.; Xu, W.; Xiao, J.; Williford, R. E. Ambient operation of Li/air batteries. *J. Power Sources* **2010**, *195*, 4332–4337.

(9) Read, J.; Mutolo, K.; Ervin, M.; Behl, W.; Wolfenstine, J.; Driedger, A.; Foster, D. Oxygen transport properties of organic electrolytes and performance of lithium/oxygen battery. *J. Electrochem. Soc.* **2003**, *150*, A1351–A1356.

(10) Débart, A.; Paterson, A. J.; Bao, J.; Bruce, P. G. α-MnO2 nanowires: a catalyst for the O_2 electrode in rechargeable lithium batteries. *Angew. Chem., Int. Ed.* **2008**, *47*, 4521–4524.

(11) Xu, W.; Xiao, J.; Zhang, J.; Wang, D.; Zhang, J.-G. Optimization of nonaqueous electrolytes for primary lithium/air batteries operated in ambient environment. *J. Electrochem. Soc.* **2009**, *156*, A773–A779.

(12) Xiao, J.; Xu, W.; Wang, D.; Zhang, J.-G. Optimization of air electrode for Li/air batteries. *J. Electrochem. Soc.* **2010**, *157*, A487–A492.

(13) Kuboki, T.; Okuyama, T.; Ohsaki, T.; Takami, N. Lithium-air batteries using hydrophobic room temperature ionic liquid electrolyte. *J. Power Sources* **2005**, *146*, 766–769.

(14) Beattie, S. D.; Manolescu, D. M.; Blair, S. L. High capacity lithium-air cathodes. *J. Electrochem. Soc.* **2009**, *156*, A44–A47.

(15) Xiao, J.; Xu, W.; Wang, D.; Zhang, J.-G. Hybrid air-electrode for Li/air Batteries. *J. Electrochem. Soc.* **2010**, *157*, A294–A297.

(16) Punckt, C.; Pope, M. A.; Liu, J.; Lin, Y. H.; Aksay, I. A. Electrochemical performance of graphene as effected by electrode porosity and graphene functionalization. *Electroanalysis* **2010**, *22*, 2834–2841.

(17) Liu, C.; Yu, Z.; Neff, D.; Zhamu, A.; Jang, B. Graphene-based supercapacitor with anultrahigh energy density. *Nano Lett.* **2010**, *10*, 4863–4868.

(18) Wang, D.; Choi, D.; Li., J.; Yang, Z.; Nie, Z.; Kou, R.; Hu., D.; Wang, C.; Saraf, L. V.; Zhang, J.; Aksay, I. A.; Liu, J. Self-assembled TiO_2-graphene hybrid nanostructures for enhanced Li-ion insertion. *ACS Nano* **2009**, *3*, 907–914.

(19) Kou, R.; Shao, Y.; Mei, D.; Nie, Z.; Wang, D.; Wang, C.; Visvanathan, V. V.; Park, S.; Aksay, I. A.; Lin, Y.; Wang, Y.; Liu, J. Stabilization of electrocatalytic metal nanoparticles at metal-metal oxide-graphene triple junction points. *J. Am. Chem. Soc.* **2011**.

(20) Yoo, E.; Zhou, H. Li−air rechargeable battery based on metal-free graphene nanosheet catalysts. *ACS Nano* **2011**, *5*, 3020–3026.

(21) Schniepp, H. C.; Li, J. L.; McAllister, M. J.; Sai, H.; Herrera-Alonso, M.; Adamson, D. H.; Prud'homme, R. K.; Car, R.; Saville, D. A.; Aksay, I. A. Functionalized single graphene sheets derived from splitting graphite oxide. *J. Phys. Chem. B* **2006**, *110*, 8535–8539.

(22) McAllister, M. J.; Li, J. L.; Adamson, D. H.; Schniepp, H. C.; Abdala, A. A.; Liu, J.; Herrera-Alonso, M.; Milius, D. L.; Car, R.; Prud'homme, R. K.; Aksay, I. A. Single sheet functionalized graphene by oxidation and thermal expansion of graphite. *Chem. Mater.* **2007**, *19*, 4396–4404.

(23) Novoselov, K. S.; Geim, A. K.; Morozov, S. V.; Jiang, D.; Zhang, Y.; Dubonos, S. V.; Grigorieva, I. V.; Firsov, A. A. Electric field effect in atomically thin carbon films. *Science* **2004**, *306*, 666–669.

(24) Kudin, K. N.; Ozbas, B.; Schniepp, H. C.; Prud'homme, R. K.; Aksay, I. A.; Car, R. Raman spectra of graphite oxide and functionalized graphene sheets. *Nano Lett.* **2008**, *8*, 36–41.

(25) Soboleva, T. *ACS Appl. Mater. Interfaces* **2010**, *2*, 375–384.

(26) Kruk, M. *Adsorption* **2000**, *6*, 47–51.

(27) Johnson, C. S.; Li, N.; Lefief, C.; Vaughey, J. T.; Thackeray, M. M. Synthesis, characterization and electrochemistry of lithium battery electrodes: $x\mathrm{Li_2MnO_3}\cdot(1-x)\mathrm{LiMn_{0.333}Ni_{0.333}Co_{0.333}O_2}$ $(0 \le x \le 0.7)$. *Chem. Mater.* **2008**, *20*, 6095–6106.

(28) Fergus, J. W. Recent developments in cathode materials for lithium ion batteries. *J. Power Sources* **2010**, *195*, 939–954.

(29) Yang, X.; Xia, Y. The effect of oxygen pressures on the electrochemical profile of lithium/oxygen battery. *J. Solid State Electrochem.* **2010**, *14*, 109–114.

(30) Freunberger, S. A.; Chen, Y.; Peng, Z.; Griffin, J. M.; Hardwick, L. J.; Bardé, F.; Novák, P.; Bruce, P. G. Reactions in the rechargeable lithium-O_2 battery with alkyl carbonate electrolytes. *J. Am. Chem. Soc.* **2011**, *133*, 8040–8047.

(31) Xiao, J.; Hu, J.; Wang, D.; Hu, D.; Xu, W.; Graff, G. L.; Nie, Z.; Liu, J.; Zhang, J.-G. Investigation of the rechargeability of Li−O_2 batteries in non-aqueous electrolyte. *J. Power Sources* **2011**, *196*, 5674–5678.

(32) Peng, Z. Q.; Freunberger, S. A.; Hardwick, L. J.; Chen, Y. H.; Giordani, V.; Bard, F.; Novak, P.; Graham, D.; Tarascon, J. M.; Bruce, P. G. Oxygen reactions in a non-aqueous Li^+ electrolyte. *Angew. Chem., Int. Ed.* **2011**, *50*, 6351–6355.

(33) Laoire, C. Ó; Mukerjee, S.; Plichta, E. J.; Hendrickson, M. A.; Abraham, K. M. Rechargeable lithium/TEGDME-$LiPF_6$/O_2 battery. *J. Electrochem. Soc.* **2011**, *158* (3), A302–A308.

(34) Wang, D.; Xiao, J.; Xu, W.; Zhang, J.-G. High capacity pouch-type Li−air batteries. *J. Electrochem. Soc.* **2010**, *157*, A760–A764.

(35) Xu, W.; Viswanathan, V. V.; Wang, D.; Towne, S. A.; Xiao, J.; Nie, Z.; Hu, D.; Zhang, J.-G. Investigation on the charging process of Li_2O_2-based air electrodes in Li−O_2 batteries with organic carbonate electrolytes. *J. Power Sources* **2011**, *196*, 3894–3899.

(36) Gopalakrishnan, G.; McCloskey, B. Investigating the electrochemistry of Li-O_2 battery using DEMS and surface characterization techniques. *Symposium on Scalable Energy Storage Beyond Lithium III: Materials Perspectives*, Oak Ridge, TN, 2010.

(37) Kresse, G.; Furthmuller, J. Efficient iterative schemes for *ab initio* total-energy calculations using a plane-wave basis set. *Phys. Rev. B* **1996**, *54*, 11169–11186.

(38) Kresse, G.; Furthmuller, J. Efficiency of ab initio total energy calculations for metals and semiconductors using a plane-wave basis set. *Comput. Mater. Sci.* **1996**, *6*, 15–50.

(39) Hummelshoj, J. S.; Blomqvist, J.; Datta, S.; Vegge, T.; Rossmeisl, J.; Thygesen, K. S.; Luntz, A. C.; Jacobsen, K. W.; Norskov, J. K. Communications: Elementary oxygen electrode reactions in the aprotic Li−air battery. *J. Chem. Phys.* **2010**, *132*, 071101.

(40) Mei, D. H.; Ge, Q. F.; Kwak, J. H.; Kim, D. H.; Szanyi, J.; Peden, C. H. F. Adsorption and formation of BaO overlayers on γ-Al_2O_3 Surfaces. *J. Phys. Chem. C* **2008**, *112*, 18050–18060.

(41) Blochl, P. E. Projector augumented-wave method. *Phys. Rev. B* **1994**, *50*, 17953–17979.

(42) Kresse, G.; Joubert, D. From ultrasoft pseudopotentials to the projector augmented-wave method. *Phys. Rev. B* **1999**, *59*, 1758–1775.

(43) Perdew, J. P.; Burke, K.; Ernzerhof, M. Generalized gradient approximation made simple. *Phys. Rev. Lett.* **1996**, *77*, 3865–3868.

(44) Lee, G. D.; Wang, C. Z.; Yoon, E.; Hwang, N. M.; Kim, D. Y.; Ho, K. M. Diffusion, coalescence, and reconstruction of vacancy defects in graphene layers. *Phys. Rev. Lett.* **2005**, *95*, 205501–205504.